RESEARCH ARTICLE

The role of shallow convection in the momentum budget of the trades from large-eddy-simulation hindcasts

Kevin C. Helfer[1] | **Louise Nuijens**[1] | **Vishal Dixit**[1]

[1]Department of Geoscience and Remote Sensing, Delft University of Technology, Delft, The Netherlands

Correspondence
K. C. Helfer, Delft University of Technology, Stevinweg 1, 2628CN Delft, The Netherlands
Email: k.c.helfer@tudelft.nl

Funding information
This project has received funding from the European Research Council (ERC) under the European Union's Horizon 2020 research and innovation programme (Starting grant agreement no. 714918).

Motivated by the abundance of low clouds in the subtropics, where the easterly trade winds prevail, we study the role of shallow convection in the momentum budget of the trades. To this end, we use ICON-LEM hindcasts run over the North Atlantic for twelve days corresponding to the NARVAL1 (winter) and NARVAL2 (summer) flight campaigns. The simulation protocol consists of several nested domains, and we focus on the inner domains ($\approx 100 \times 100$ km^2) that have been run at resolutions of 150–600 m, which are subjected to a realistically varying flow that has developed in the outer domain. Combined, the resolved advection and the subgrid stresses decelerate the easterly flow from the surface up to about 2 km in winter and 1 km in summer, a result that is insensitive to horizontal resolution. The unresolved processes are strongest near surface and are well captured by traditional K-diffusion theory, but convective-scale motions that are not considered in K-diffusion theory contribute the most in the upper part of mixed layer and are strongest just below cloud base. The results point out that convection in the mixed-layer — the roots of trade-wind cumuli and subcloud layer circulations — play an important role in slowing down easterly flow below cloud base (but little in the cloud layer itself), which helps make the zonal wind jet more distinct. Most of the friction within the clouds

and near the wind jet stems from smaller-scale turbulence stresses.

KEYWORDS
trade winds, momentum budget, convective momentum transport, shallow convection, large-eddy simulation, K-diffusion

1 | INTRODUCTION

The trade winds are easterly winds that prevail over the tropical and subtropical oceans north and south of the equator. They form the inflow branches of the large-scale Hadley circulation and influence patterns of convergence and tropical rainfall. Furthermore, they modulate turbulent heat fluxes and stresses at the sea surface, and through these sea-surface temperatures and ocean mixing. Therefore, it is important to understand the structure of the trade winds and the processes that influence this structure. One of those processes is shallow convection, which leads to ubiquitous cumulus clouds across the trades and has long been known to play an important role in setting boundary-layer temperature and humidity (Riehl et al., 1951; Malkus, 1958; Tiedtke et al., 1988; Neggers et al., 2007). However, its role in the horizontal momentum budget, such as whether it contributes to a frictional force for example by mixing slow near-surface momentum upwards, is not well understood.

Most studies focusing on the vertical structure of the wind in the trades stem several decades ago, such as the study by Riehl et al. (1951) using WWII weather ship data collected in the North Pacific and the momentum budget reconstructions using radiosonde arrays from the Barbados Oceanographic and Meteorological Experiment (BOMEX; Holland and Rasmusson, 1973) and the Atlantic Tradewind Experiment (ATEX; Augstein et al., 1974; Brümmer et al., 1974). In these studies the frictional force arising from Reynolds stresses is derived as a residual from other terms in the momentum budget, e.g. the large-scale advection, pressure-gradient and Coriolis forces. In their reconstruction of the momentum budget during ATEX, Brümmer et al. (1974) in particular pointed out that turbulent stresses do not vanish at the mixed-layer top or base of the cloud layer. They hypothesized that an additional source of stress could stem from convection, which would help explain discrepancies between derived and measured surface-drag coefficients.

A similar point has been made by studies that explain patterns of surface winds over tropical oceans. Traditionally, tropical surface winds have been explained using Rayleigh damping models that take the generalised Ekman balance as a starting point (e.g. Deser, 1993). These models assume a balance between pressure gradients, Coriolis acceleration and friction:

$$f\mathbf{k}\times\overline{\mathbf{u}} + \frac{1}{\rho_0}\nabla\overline{p} = \frac{\partial\tau}{\partial z}, \tag{1}$$

where f is the Coriolis parameter, $\mathbf{u}$ is the wind vector, ρ_0 is a reference density, p is the pressure and τ is the stress tensor. These models neglect viscosity and model the friction as a linear function of the surface wind speed ($\partial_z\tau = -\eta\mathbf{U}$) that goes to zero at the top of the boundary layer, which in the tropics is typically taken as the subcloud layer. The latter implies that there is no vertical mixing of momentum at the boundary-layer top that can play a role in setting surface (and boundary) layer winds. However, using the mixed-layer model to model boundary-layer winds, Stevens et al. (2002) and Back and Bretherton (2009) demonstrate that the acceleration of near-surface winds by mixing momentum between the boundary layer and the free troposphere is key at explaining the climatology of surface

winds in the tropics. The mixed-layer model does not explicitly take into account convective momentum transport (CMT), but a convective mass flux is implicit in the formulation of an entrainment or exchange flux at the mixed-layer (boundary-layer) top. In another study, Carr and Bretherton (2001) derived CMT as a residual from the large-scale budget of momentum using reanalysis data and found CMT to be larger in the lower troposphere than in the upper troposphere, suggesting that the abundance of shallow convection could lead to a source of shallow CMT that would be important for large-scale circulations.

In none of these studies, the relative influence of small-scale turbulence versus more coherent thermal plumes associated with convection on the total momentum transport within the boundary layer is specifically analysed. This is the objective of our study, in which we ask: What is the role of shallow convection in the momentum budget of the trades? We also address whether moist convection contributes meaningfully to turbulent stresses at the mixed-layer top (approximately cloud base) and whether the profile of the momentum flux $\partial_z \tau$ within the well-mixed subcloud layer behaves according to the established K-diffusion model.

To do so, we make use of a unique set of high-resolution simulations run with the ICON-LEM model in hindcast mode over a domain spanning the entire North Atlantic trades (Stevens et al., 2019). Unlike traditional LES cases, these hindcasts are initialized and forced with ECMWF analysis data at the outer domain boundaries, so that smaller inner domains on the order of a few 100×100 km^2 feel a realistically varying large-scale state with air masses moving in at one boundary and moving out at the other — as opposed to the traditionally used periodic boundary conditions. The dataset covers twelve days in both summer and winter with a variety of atmospheric states and cloud regimes, including days with shallow and more deep convection. The inner domains have been run with different resolutions, which allows us to infer the importance of eddies of different scales.

This paper is structured as follows: We first describe the ICON-LEM simulations and our analysis of the momentum budget (Section 2). In Section 3, we analyse the momentum budget for winter and summer days and look closer at the role of shallow convection versus small-scale turbulence in setting the frictional force, in particular. Section 4 discusses the momentum flux and how it relates to the K-diffusion model. Finally, we summarise our findings in Section 5.

2 | DATA DESCRIPTION

We analysed large-eddy-simulation (LES) hindcasts that were performed on specific days of the Next-Generation Advanced Remote Sensing for Validation (NARVAL) expeditions (Stevens et al., 2019), using the Icosahedral Nonhydrostatic (ICON) model (Zängl et al., 2015) as an LES (ICON-LEM; Dipankar et al., 2015). These simulations cover an extensive part of the tropical North Atlantic (Fig. 1). Six days in December 2013 and six days in August 2016 have been simulated (Table 1). The simulation protocol consisted of five nested domains that decrease both in size and in horizontal grid spacing from 600 m over 300 m to 150 m (Fig. 1); the domains were coupled via a one-way nesting. Here, we only consider the three smallest domains, which used LES physics, while the two largest domains used NWP physics (discussed by Klocke et al., 2017). The LES runs were initialised at 0900 UTC each day, using data from the larger domains, which in turn were initialised using ECMWF analysis data and forced at the outermost boundaries using three-hourly ECMWF forecasts. The model was then run for 27 hours, whereby the first three hours were disregarded as model spin-up. We emphasise that the modelling approach here is unlike typical idealised LES studies. In particular, there were no periodic boundary conditions, subsidence was not prescribed and the runs were not initialised with laterally homogeneous profiles. Further details can be found in Stevens et al. (2019). Here, we consider an area of $1^\circ \times 1^\circ$ ($\approx 100 \times 100$ km^2) east of Barbados (58–59° W, 12.6–13.6° N; orange square in Fig. 1), which is

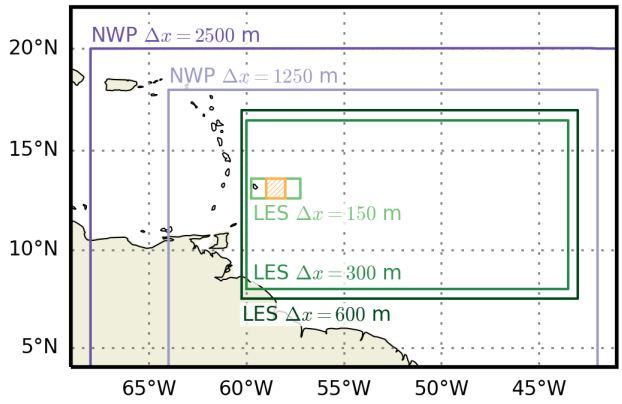

FIGURE 1 Overview of the simulation protocol of Stevens et al. (2019) with two outer domains that use NWP physics (purple) and three inner domains that use LES physics (green). The domains are coupled via a one-way nesting, and the horizontal resolution Δx increases as the domain size decreases. The hatched orange square indicates the area of interest of the present paper.

similar to a typical general-circulation-model grid box and coincides with the main operational area of the EUREC^{4}A field campaign that took place in early 2020 (Bony et al., 2017).

Within that area, we calculated all contributions to the horizontal momentum equation at every grid point of the LES output, which is available every 15 minutes. The LES solves the filtered Boussinesq-approximated Navier-Stokes equation, which for the horizontal wind components reads (e.g. Stull, 1988):

$$\frac{\partial \tilde{u}_i}{\partial t} = \underbrace{f \varepsilon_{ij3} \tilde{u}_j}_{C} \underbrace{- \frac{1}{\rho} \frac{\partial p}{\partial x_i}}_{P} \underbrace{- \tilde{u_j} \frac{\partial \tilde{u}_i}{\partial x_j}}_{A} \underbrace{- \frac{\partial \tau_{ij}}{\partial x_j}}_{R}, \tag{2}$$

where the tildes $\tilde{}$ indicate the LES-filtered variables, u_i are the horizontal wind components in the x- and y-direction ($i = 1, 2$), f is the Coriolis parameter, ε_{ij3} is the Levi-Civita symbol, ρ is the density, p is the pressure and τ_{ij} is the subgrid stress tensor. (In the following, we drop the tildes for convenience.) The first term on the right-hand side of the equation depicts the Coriolis effect (C), the second the pressure-gradient force (P) and the third the resolved advection (A), which may be decomposed into a horizontal and a vertical component:

$$\underbrace{-u_j \frac{\partial u_i}{\partial x_j}}_{A} = \underbrace{-u \frac{\partial u_i}{\partial x} - v \frac{\partial u_i}{\partial y}}_{A_h} \underbrace{- w \frac{\partial u_i}{\partial z}}_{A_v}. \tag{3}$$

The fifth term of Eq. 2 corresponds to stresses introduced on scales smaller than the model grid: the subgrid turbulence in LES, calculated using a Smagorinsky turbulence scheme. This term is calculated as a residual R, while output of the subgrid tendencies or fluxes (apart from the surface fluxes) are not available. We remark that due to ICON's triangular grid the exact form of the Navier-Stokes equation solved by the model is slightly different, though the principles discussed before still hold (see Dipankar et al., 2015).

All terms were computed using second-order central differences. The storage term on the left-hand side of the

TABLE 1 Overview of the simulated days

Campaign	Research flight	Date
NARVAL1	RF 2	11 Dec. 2013
	RF 3	12 Dec. 2013
	RF 4	14 Dec. 2013
	RF 5	15 Dec. 2013
	RF 6	16 Dec. 2013
	RF 8	20 Dec. 2013
NARVAL2	RF 2	10 Aug. 2016
	RF 3	12 Aug. 2016
	RF 5	17 Aug. 2016
	RF 6	19 Aug. 2016
	RF 7	22 Aug. 2016
	RF 8	24 Aug. 2016

equation was calculated as the temporal derivative of the outputted wind field. We then spatially averaged each term of Eq. 2 on each model level over the whole $1^\circ \times 1^\circ$ area. These spatial averages were consecutively averaged over six two-hour periods (1200–1400 UTC, 1600–1800 UTC and so on until 0800–1000 UTC of the following day) of each of the twelve simulation days. This gave us a reliable statistical basis for our analysis of the mean momentum budget, while keeping the computational demand in check. Furthermore, by analysing the budget throughout the day, we were mindful of the diurnal cycle that is present even over the ocean (Vial et al., 2019). Mesoscale variability that can introduce large hourly variations are beyond the scope of this study.

3 | THE MOMENTUM BUDGET

3.1 | Mean state of winter and summer NARVAL days

The area upstream of Barbados is governed by two distinct seasons: a wet season from about June until November and a dry season throughout the rest of the year (Brueck et al., 2015). These seasons are tied to the location of the inter-tropical convergence zone (ITCZ). In the dry season, the ITCZ is located at lower latitudes, and the area east of Barbados experiences steady trade winds from east to north-east, moderate large-scale subsidence and an inversion at around 800 hPa visible in profiles of both temperature and relative humidity. In contrast to this, in the wet season, the ITCZ is located much closer to Barbados, leading to weaker winds from the east (at times even south-east), moderate upward motion and a less-defined trade inversion.

Figure 2 showcases these differences between August (red lines) and December days (blue lines): typical trade-wind conditions with shallow convection in boreal winter and deeper convection in boreal summer. The figure shows two-hour averages as thin lines and the mean over all winter days as thick blue lines and all summer days as thick red lines. In December, we have a trade-wind layer with a clear inversion, trade winds from east-north-east at the surface and a cloud fraction profile that always has a maximum just above cloud base and frequently also near the

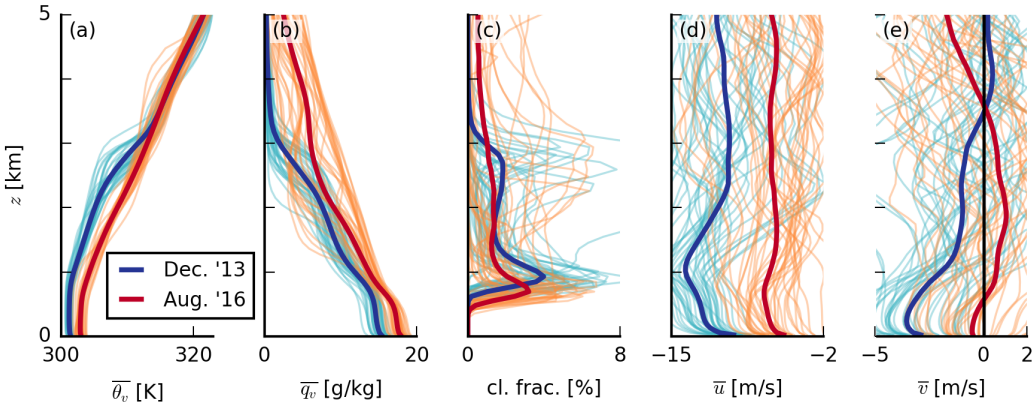

FIGURE 2 Slab-averaged profiles of (a) virtual potential temperature θ_v, (b) water vapour specific humidity q_v, (c) cloud fraction, (d) zonal wind speed u and (e) meridional wind speed v. The thin lines indicate 2-hour averages and the thick lines indicate averages over all simulated days in December (blue) and August (red).

trade-wind inversion. Such a cloud fraction profile is typical for the winter trades near Barbados where shallow cumuli are often accompanied by a stratiform cloud layer near the trade-wind inversion (Nuijens et al., 2014). On average, the December cloud fraction maximum in our simulations is around 4 percent, which is also in line with the observations of Nuijens et al. (2014). In August, the boundary layer is somewhat warmer and moister without an inversion, surface winds are much weaker and from the east, and the cloud fraction profile often has only one maximum near cloud base as well as higher cloud tops.

The typical wind profile in the North Atlantic trades is dominated by the zonal component and is characterised by steady easterlies to north-easterlies near the surface, a wind speed maximum near cloud base and decreasing wind speed further aloft (e.g. Holland and Rasmusson, 1973; Brümmer et al., 1974; Brueck et al., 2015). Figure 2d shows that we find most of these features on the simulated days. In particular, the dominance of the zonal component and the wind speed maximum near cloud base are well captured during winter. An important difference between the wind as calculated from the simulation output to for example the BOMEX wind profile is the wind above 2.5 km: While in BOMEX the zonal wind speed continues to decrease with height (i.e. become less negative) (Holland and Rasmusson, 1973), the mean zonal wind during NARVAL is approximately constant with height. Such a near-constant wind with height is not typical on individual days, but reflects the large high day-to-day variability in wind shear at those levels.

We define the wind turning angle as the difference between the actual wind direction and the geostrophic wind direction and show it in Fig. 3 together with the total wind speed and the wind direction. In winter, the wind turning angle is negative near the surface and decreases to zero throughout a layer of about 1.5 km deep. The negative angle indicates that the actual wind comes from the north-east, rather than from the east, which implies that the wind has turned across isobars towards lower pressure at the equator, as identified in earlier studies of (sub)tropical winds (Brümmer et al., 1974; Stevens et al., 2002). In summer, there is much more variability in the wind turning and an ageostrophic wind component is more common even at greater heights. This would be in line with slow momentum from near the surface being transported across a deeper layer in summer due to deeper convection, introducing a so-called 'cumulus friction'. In the next sections, we look closer at the different processes in the momentum budget to identify the role of convection.

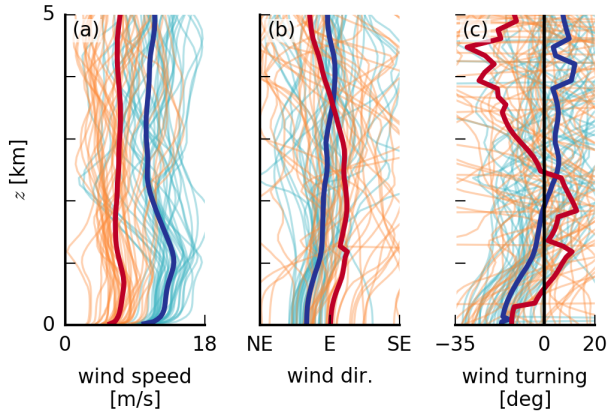

FIGURE 3 Slab-averaged profiles of (a) total wind speed, (b) wind direction and (c) wind turning (with respect to purely geostrophic flow). A negative wind turning angle here means more northerly wind and a positive angle more southerly wind. The line types and colours are the same as in Fig. 2.

3.2 | Momentum tendencies

The different momentum tendencies as defined in Eq. 2 are shown in Fig. 4 with the means for winter and summer separately. The top row shows the zonal component and the bottom row the meridional component. All tendencies except for the residual show significant variability in both sign and magnitude in the two-hourly profiles (thin lines in Fig. 4). However, on average, the storage term is negligible at all heights. The pressure gradient dominates in the north–south direction (Fig. 4h) and is largely balanced by the Coriolis force (Fig. 4g), which leads to the development of predominantly zonal flow. All forces are much weaker in summer than in winter, caused by the weaker pressure-gradient force (Fig. 4h, in red) due to the northward wander of the ITCZ.

The resolved advective tendency and the residual tendency (Fig. 4d-e, i-j) exhibit large values in the lower 2 km of the atmosphere, whereas above 2 km they are on average negligible. The advective tendency includes all motions on scales equal to and larger than the model grid, whereas the residual tendency is interpreted as subgrid turbulence not resolved by the model grid. These two mostly act in the opposite direction. For instance, the advective tendency is negative close to the surface in both wind components, which indicates an acceleration in the direction of the mean north-easterly wind, whereas the residual tendency is positive, which indicates a deceleration in the direction of the mean wind.

Perhaps the vectors in Fig. 5 offer a more intuitive view of these results. The top row shows the direction of the wind, the pressure gradient and Coriolis force, as well as the forcing from the advection and residual tendencies combined, using a vector representation for winter (blue) and summer (red). The vectors are shown at different height levels: (a) in the surface layer, (b) well into the mixed layer, (c) near cloud base and (d) at the zonal wind jet in the cloud layer. This vector view shows more clearly that the combined vector $A + R$ is not simply opposing the mean surface wind. This implies that the winds do not just feel friction from the surface. Mixing across the boundary layer may introduce air masses whose wind is closer to geostrophy, thereby reducing the turning across isobars (Brümmer et al., 1974; Stevens et al., 2002). The bottom panel separates the advective from the residual tendencies, and shows that near the surface, the subgrid turbulence (R) is as expected directed almost opposite to the mean wind, whereas the resolved flow (A) is aligned with the mean wind. In the mixed layer (400 m) A is instead directed against the mean

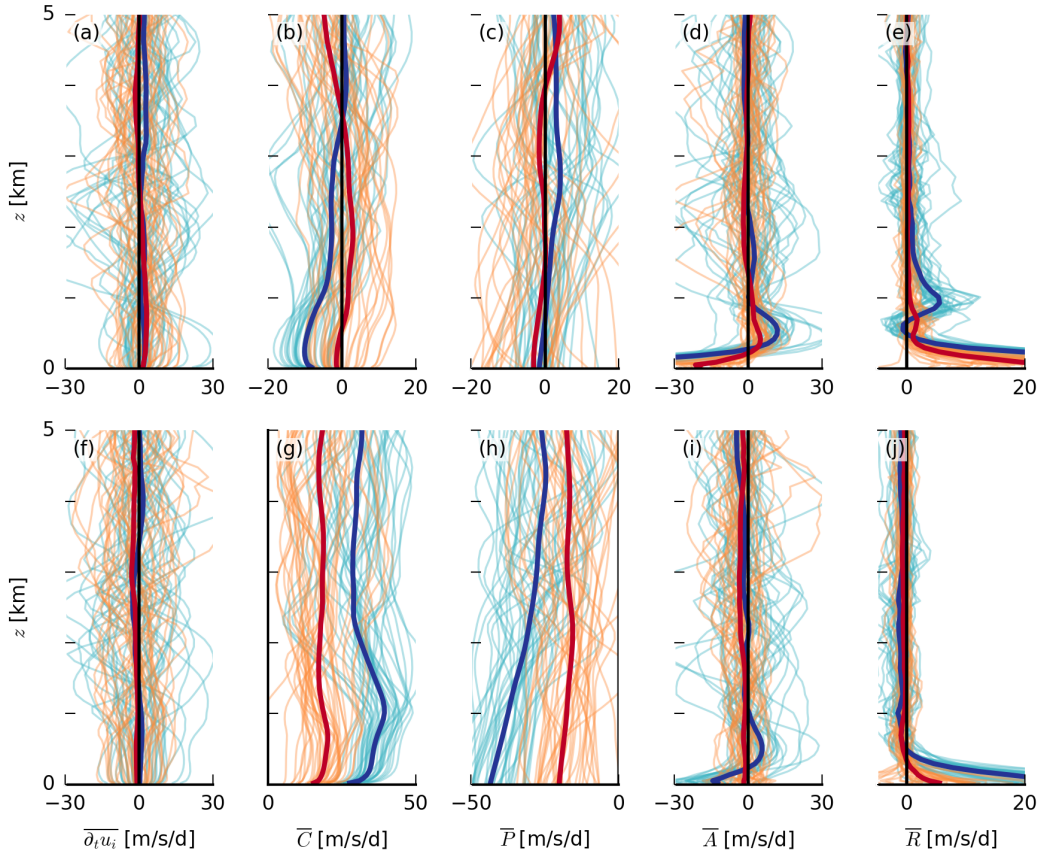

FIGURE 4 Slab-averaged profiles of the terms of the momentum budget (cf. Eq. 2) for (a–e) the zonal wind component and (f–j) the meridional component: (a, f) total tendency $\partial_t u_i$, (b, g) Coriolis force C, (c, h) pressure-gradient force P, (d, i) resolved advection A and (e, j) residual R. The line types and colours are the same as in Fig. 2.

wind, and maximizes near cloud base (Fig. 4d, i). In other words, advection here tends to reduce the easterly wind component. In the lower cloud layer, near the zonal wind jet (~1 km), the advective tendency is closer to zero, only to become slightly positive in the cloud layer between 1 and 2 km (Fig. 4d, i). In the lower cloud layer the subgrid turbulence R is again larger with positive values, but only in winter, presumably because the zonal wind jet and thus shear is more pronounced (Fig. 4e, j; Fig. 5c,d). Combined, $A + R$ have a considerable magnitude at cloud base, which is at least a third of $A + R$ present near the surface.

The advective tendency includes contributions from resolved horizontal and vertical advection (Eq. 3). In Fig. 6a–b, g–h, the horizontal and vertical component A_h and A_v of the total advection are shown. The structure of the total advective tendency (Fig. 4e) is similar to that of A_h, which acts to accelerate the flow near the surface and slow down the flow in the mixed layer and near cloud base (Fig. 6a, f). Vertical advection A_v partially balances these tendencies (Fig. 6b, g). We may ask what the contribution of large-scale wind gradients (both horizontal and vertical) acting on

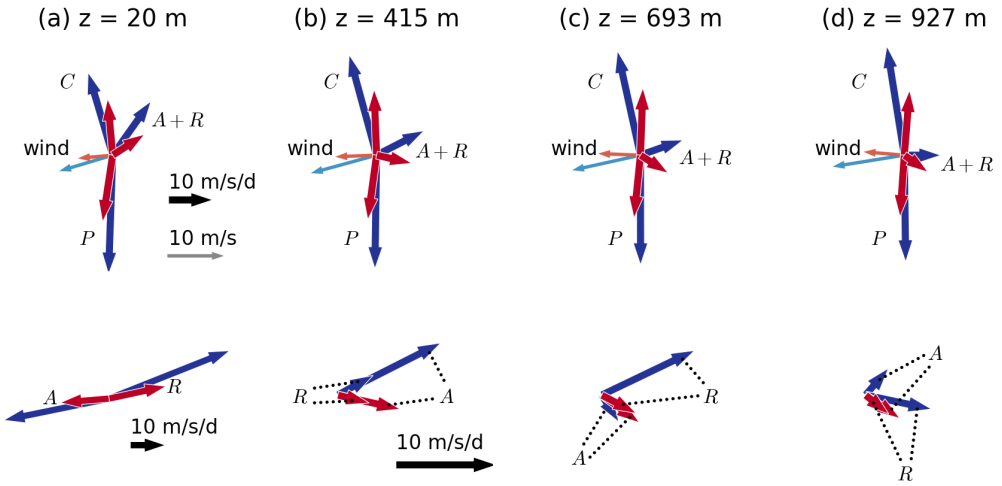

FIGURE 5 Vector representation of the momentum budget averaged over (blue) all December days and (red) all August days (a) near the surface (~ 20 m), (b) in the mixed layer (~ 400 m), (c) near cloud base (~ 700 m) and in the cloud layer (~ 900 m). The thinner arrows indicate the wind speed and direction at each height level. The scale is the same for the whole top row but different for the panels in the bottom row, as indicated by the black and grey arrows.

the mean wind is. Using a Reynolds decomposition of the wind into a mean and a fluctuating part ($u_i = \overline{u_i} + u_i'$), the domain-mean advection of the zonal wind may be written as:

$$\overline{u\frac{\partial u}{\partial x} + v\frac{\partial u}{\partial y} + w\frac{\partial u}{\partial z}} \approx \overline{u}\frac{\partial \overline{u}}{\partial x} + \overline{v}\frac{\partial \overline{u}}{\partial y} + \overline{w}\frac{\partial \overline{u}}{\partial z} + \overline{u'\frac{\partial u'}{\partial x}} + \overline{v'\frac{\partial u'}{\partial y}} + \overline{w'\frac{\partial u'}{\partial z}} \tag{4}$$

The first three terms on the right-hand side represent large-scale advection and the last three terms the advection through turbulent flows. In absence of an estimate of the large-scale horizontal wind gradient, we may estimate the contribution from 'large scales' by applying a high-pass filter with a cutoff scale of 10 km and then calculate the horizontal advective tendency $A_{ls,h}$, which is plotted in Fig. 6c and i. The large-scale vertical advection may be estimated from the product of the domain-mean vertical velocity and the vertical gradient of horizontal wind, which is shown in Fig. 6d and j. Neither of the large-scale terms have a systematic structure and sign in the lower atmosphere, with large hour-to-hour variations, which on average are close to zero. This implies that horizontal wind fluctuations ($\overline{u'\partial_x u'} + \overline{v'\partial_y u'} + \overline{w'\partial_z u'}$) on scales smaller than 10 km (i.e. convection and turbulence rather than large-scale circulations) dominate the advective tendencies.

As in Fig. 5, we may combine the advection and residual into one term ($A + R$, Fig. 6d, i) and the same for the pressure-gradient and Coriolis forces ($P + C$, Fig. 6e, j). The two terms mirror nicely, which reflects the overall balanced budget (Fig. 4a, f). This also more clearly reveals the depth of the frictional layer, which we interpret as the layer where the dominant easterlies are decelerated, which extends up to about 2 km in winter and 1 km during summer. Thinking about the concept of cumulus friction (Schneider and Lindzen, 1976) in studies of deep convection, it appears that there is a friction between 1 and 2 km that is about a third of the value in the well-mixed subcloud layer. This is not surprising because of the strong turbulence associated with the clouds at these altitudes. This seems a good point to investigate the momentum fluxes in more detail, as well as the sensitivity of these results to horizontal resolution.

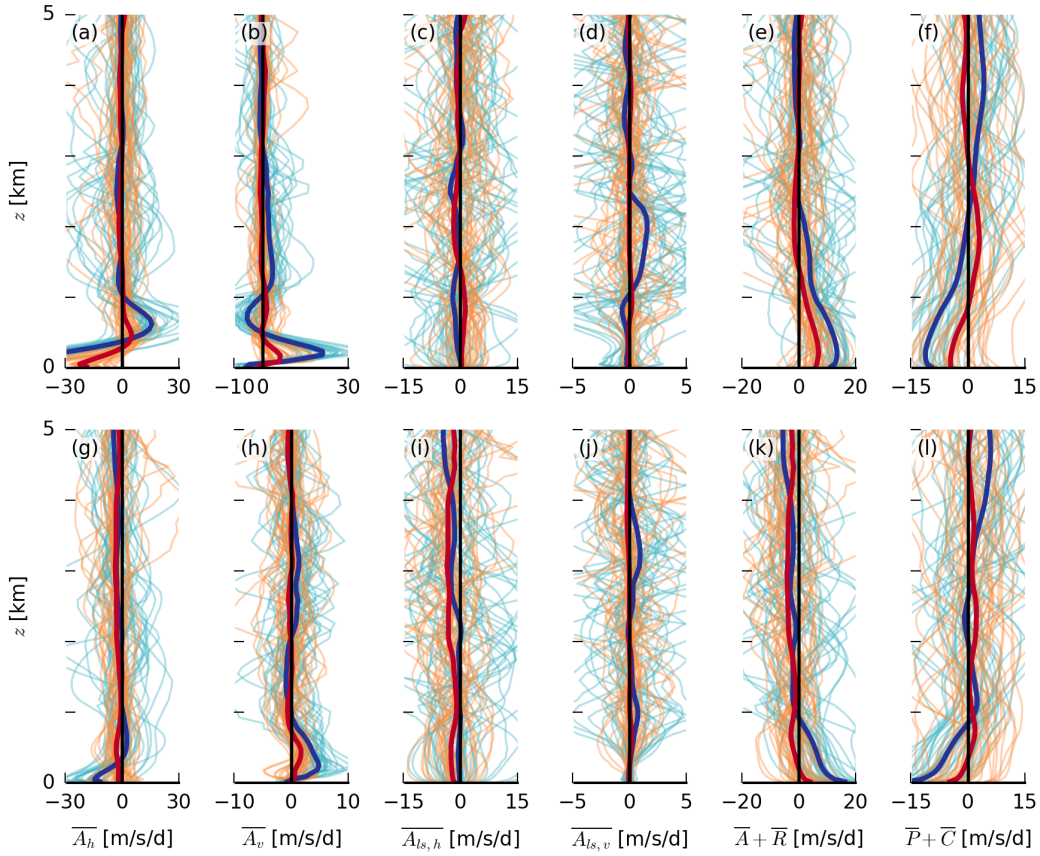

FIGURE 6 Slab-averaged profiles of (a, g) horizontal and (b, h) vertical advection, A_h and A_v, respectively, (c, i) large-scale horizontal and (d, j) large-scale vertical advection, $A_{ls,h}$ and $A_{ls,v}$, respectively, (e, k) the sum of total resolved advection and residual $A + R$ and (f, l) the sum of pressure-gradient and coriolis force $P + C$ for (a–f) the zonal wind component and (g–l) the meridional component. The line types and colours are the same as in Fig. 2.

3.3 | Resolved momentum fluxes

Further manipulation of the Reynolds-averaged advection term (Eq. 4) shows that the divergence of the momentum flux represents the influence of turbulent stress on the mean motion (e.g. Stull, 1988):

$$\overline{u_j \frac{\partial u_i}{\partial x_j}} \approx \overline{u_j} \frac{\partial \overline{u_i}}{\partial x_j} + \frac{\partial \overline{u_i' w'}}{\partial z}. \tag{5}$$

Considering means over the entire domain, we find that the profile of the total advective tendency (Fig. 4d, i) is close to that of the vertical divergence of momentum flux (Fig. 7b, f). The resolved momentum fluxes $u'w'$ and $v'w'$ can be computed by taking the deviations from the slab-average u and v over the whole $1^\circ \times 1^\circ$ area. We may interpret these fluxes as the main contributors to what we call convective momentum transport (CMT), including dry and moist

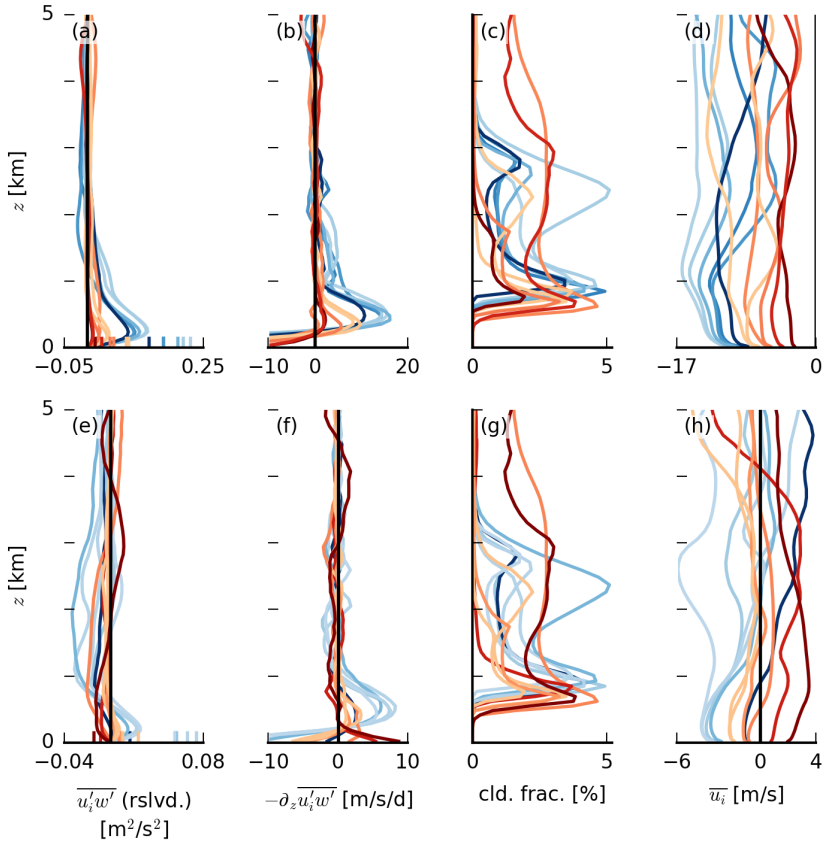

FIGURE 7 Slab-averaged daily profiles of (a, e) the momentum fluxes $u'w'$ and $v'w'$, (b, f) their negative vertical divergence $-\partial_z\overline{u'w'}$ and $-\partial_z\overline{v'w'}$, (c, g) the cloud fraction and (d, h) the zonal and meridional wind speed. In the top row the lines are coloured by surface zonal wind speed and in the bottom row by the surface meridional wind speed, where blue shades indicate winter days and red shades summer days. The coloured tick marks in (a) and (e) indicate the surface momentum fluxes.

convection on scales of 150 m and larger. Figure 7 shows the daily-averaged profiles of resolved momentum fluxes in the zonal (top row) and meridional direction (bottom row), along with their negative vertical divergence $-\partial_z \overline{u_i' w'}$. On the horizontal axis of Fig. 7a and e, the coloured tick marks correspond to the total turbulent momentum flux at the surface, which reveals the contribution of unresolved fluxes, which is generally largest near the surface. The profiles are coloured by the strength of the respective zonal and meridional surface wind speed, for winter (blue) and summer (red).

The magnitude of the momentum fluxes is largely determined by the magnitude and structure of the zonal and meridional (geostrophic) wind: Stronger surface wind speeds during winter are accompanied by larger shear in the surface and subcloud layers and larger turbulent fluxes. Above approximately 2 km the fluxes are small, even if clouds are still present at those heights (Fig. 7c). Deep convection on some of the summer days does not lead to more momentum flux at greater heights. The meridional momentum flux (Fig. 7e) is persistently negative from cloud base upwards, suggesting that faster (more negative) momentum from the near-surface meridional jet (Fig. 7h) is transported through the clouds. On two summer days with positive surface v and without a near-surface jet, the meridional momentum flux is negative even at the surface.

Near the surface, the resolved zonal flux divergence is negative, which is associated with an acceleration of easterly flow, as seen in Fig. 4d. This may be interpreted as CMT removing air masses from near the surface, where the air masses have gained a westerly wind component due to surface layer turbulent stresses. Similarly, the resolved meridional flux divergence mostly has the same sign as the surface v, indicating an acceleration of the surface wind due to CMT. At cloud base, both the zonal and the meridional flux divergences act to decelerate the flow. In the zonal component and in winter, this continues to be the case up to about 2 km. We here chose a length scale of 150 m to denote effects of CMT, but this is an artificial cut-off. Hence, in the following section, we question how these results change if we increase the length scale (horizontal resolution) to 300 or 600 m.

3.4 | Sensitivity to horizontal resolution

Our area of interest has three LES domains with different horizontal resolutions of 150, 300 and 600 m (see Fig. 1). Investigating the resolution dependency of our findings allows us to evaluate the role of unresolved motions versus resolved turbulence or convection. We find that the simulated winds and the total advective plus residual tendencies hardly change with resolution (Fig. 8a, d, f, i), which shows the large-scale forcing largely sets the frictional tendencies or perhaps that the small-scale processes cannot meaningfully feedback on the large-scale atmosphere. We wonder if this had been different if a two-way coupling between the LES and the NWP model had been used.

The tendency from resolved advection (Fig. 8b, g) and from the residual (Fig. 8c, h) do change with resolution. The differences are most pronounced as the grid is coarsened from 300 m to 600 m, which reduces the resolved zonal momentum flux in the subcloud layer to half its value (Fig. 8e) as less turbulence being resolved by the model. Furthermore, the zonal wind tendency due to advection is reduced to zero (or to slightly negative values) in the subcloud layer (Fig. 8b), where the residual takes over. Because 600 m is approximately the subcloud layer depth, this implies that overturning circulations associated with dry convection play a key role at introducing friction below and near cloud base. The deceleration of easterly winds by unresolved turbulence in the lower cloud layer is independent of resolution (Fig. 8c, h) and presumably caused by the zonal wind jet above cloud base (Fig. 8a) (and the meridional wind jet in the surface layer (Fig. 8f)), which can introduce significant shear-induced stresses.

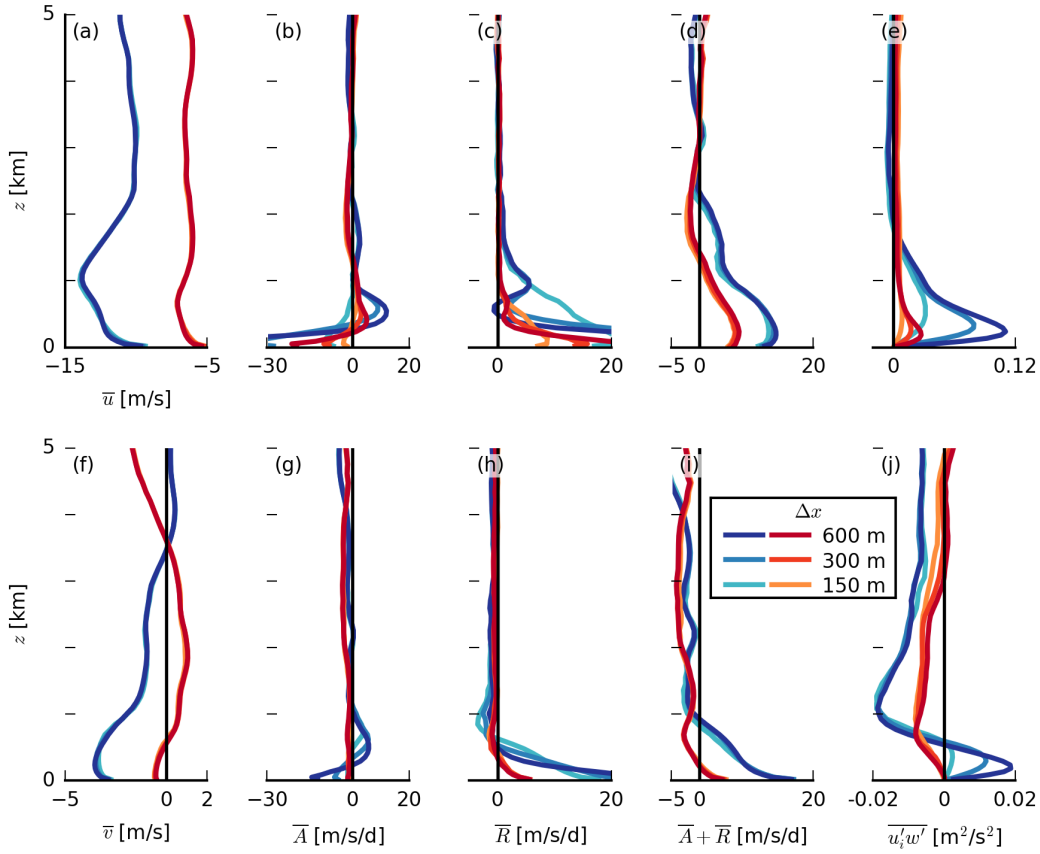

FIGURE 8 Seasonally averaged profiles of (a, f) the wind speed components u and v, (b, g) advection A, (c, h) residual R, (d, i) the sum of resolved advection and residual $A + R$ and (e, j) turbulent momentum flux $u'w'$ for different horizontal LES resolutions Δx and for (a-e) the zonal wind component and (f-j) the meridional component. Blue/cyan lines depict winter and red/orange lines summer.

3.5 | Momentum transport in moist regions

To highlight the action of moist convection in setting the momentum flux divergence, we may sample the moistest grid points using the upper quartile of the distribution of column-integrated water vapour (CWV) and contrast them with the driest quartile, presumably representing cloudy and clear sky regions, respectively. We calculate daily averaged momentum flux profiles for the individual quartiles, and average these over winter and summer days (Fig. 9a–b for winter and c–d for summer).

First, considering winter (Fig. 9a–b), we find that the momentum flux profile in the first (Q1, dry) and the second and third quartile (Q2&Q3) approaches zero at 1 km, whereas the moistest columns (Q4) have a much deeper layer of momentum flux (Fig. 9a). The differences are not due to different wind profiles, which in fact are very similar for Q1 and Q4 (Fig. 9b). Near the cloud-fraction maximum and zonal-wind jet at about 1 km, there is a thin layer in which the divergence of $u'w'$ in the moistest columns is clearly reduced, indicating a layer of only weak deceleration due to

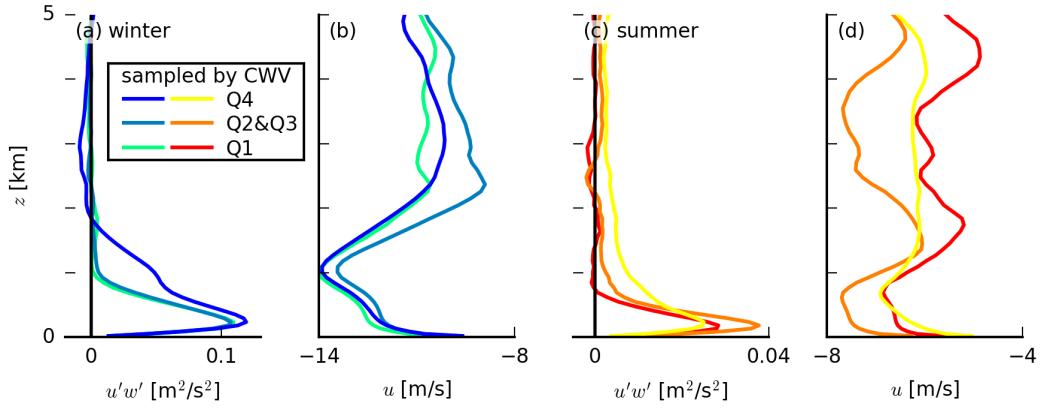

FIGURE 9 Profiles of (a, c) the zonal momentum flux $u'w'$ and (b, d) zonal wind speed averaged over quartiles of the daily column water vapour (CWV) distribution for (a–b) all December days and (c–d) all August days.

momentum transport, as also seen in Fig. 7b. Using the same ICON-LEM data, Dixit et al. (2020; in prep.) show that the momentum flux in positively buoyant updrafts is indeed constant with height or even increases with height in the lower cloud layer. In summer, we find a similar result, whereby moist quartiles with presumably deeper convection lead to the presence of positive momentum flux, but little divergence, extending far above the mixed layer (Fig. 9c).

4 | COUNTER-GRADIENT MOMENTUM TRANSPORT AND K-DIFFUSION

Coming back to our main question, *What is the role of shallow convection in the momentum budget of the trades?*, we can summarise as follows: The resolved momentum flux associated with cloud-scale and mesoscale circulations (CMT) acts to: (1) accelerate easterly flow near the surface, (2) slow down easterly flow in the upper mixed-layer and near cloud base and (3) slow down easterly flow in the cloud layer. Moreover, CMT introduces little tendency at the level of the zonal wind jet near 1 km.

Not only moist convection in the cloud layer, but also dry convection in the well-mixed subcloud layer appears to play an important role at explaining the overall frictional force. Hence, it is useful to consider what this implies for conceptual models that have demonstrated skill in explaining surface and boundary layer winds. Traditionally, turbulent momentum diffusion in the boundary layer is modelled using the so-called K-diffusion model, which assumes that momentum transport is down-gradient and acts to reduce vertical shear in the wind. In the following, we derive the turbulent diffusivity parameter from our simulations to evaluate what part of the momentum flux can be explained by down-gradient turbulent diffusion.

In K-theory, the turbulent momentum flux is modelled as the product of the turbulent diffusivity parameter K and the vertical wind gradient:

$$\tau = -\overline{u_i' w'} = K \frac{\partial \overline{u_i}}{\partial z}. \tag{6}$$

This expression can be rearranged to obtain the turbulent diffusivity parameter K for the zonal and meridional wind

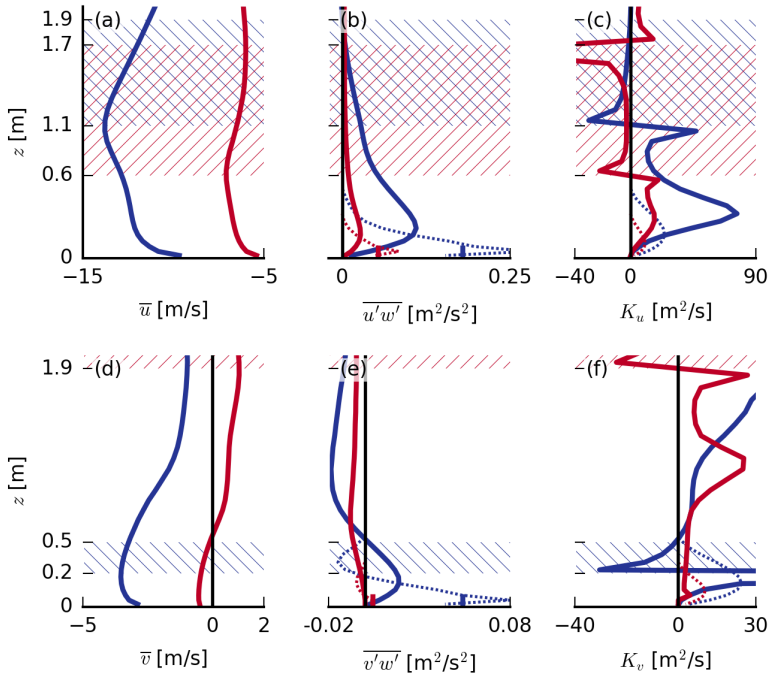

FIGURE 10 Seasonally averaged profiles of (a, d) the wind components u and v, (b, e) the momentum fluxes $u'w'$ and $v'w'$ and (c, f) the turbulent diffusivity parameter K_u and K_v (calculated as the negative ratio of momentum flux and shear; see Eq. 7). The hatching indicates altitudes where $K_i < 0$. Blue lines and hatching from top left to bottom right depict winter and red lines and hatching from top right to bottom left summer. The dotted lines in (c) and (f) indicate the K profile that is computed following Eq. 8, and the dotted lines in (b) and (e) indicate the momentum flux computed from that K (Eq. 6).

separately:

$$K_i = -\frac{\overline{u_i' w'}}{\partial_z \overline{u_i}}. \tag{7}$$

By definition, a positive K_i denotes down-gradient transport, whereby the momentum flux acts to diffuse existing gradients in wind. If $K_i < 0$, the momentum transport is counter-gradient (also referred to as up-gradient), meaning that the momentum flux acts to increase vertical gradients (shear).

Most notably, the profiles of K_i shown in Fig. 10 reveal several layers of counter-gradient momentum transport both in the zonal and the meridional components. Along with K_i, Fig. 10 (which zooms in on the lowest 2 km of the atmosphere) shows the slab-averaged wind and momentum-flux profiles. From the surface up to the zonal wind jet, turbulent flux of zonal wind is overall down-gradient, but with a notable reduction in K_u between 400 m and 1 km, i.e. near cloud base. Above the zonal wind jet, the zonal momentum transport is counter-gradient. The flux vanishes and K_u is zero above 1.7 km. Larson et al. (2019) also identified this layered structure in the zonal momentum fluxes derived from BOMEX simulations. While in Larson et al.'s BOMEX runs, the counter-gradient layer is some 300 m tick, here it is about twice as thick. In their analysis of the budget of the zonal momentum flux of these ICON-LEM

simulations, Dixit et al. (2020; in prep.) note that besides the effective buoyancy production in updrafts, horizontal circulations help increase the presence of (counter-gradient) flux in the cloud layer. However, the production of flux by horizontal circulations is negligible when sampling traditional LES domains on the order of a few 10×10 km^2, which might explain the differences between momentum fluxes in BOMEX and the NARVAL days. During boreal summer, $K_u < 0$ over an even deeper layer, but the gradient in $\overline{u}$ is only very slightly negative and the momentum flux is rather weak across that layer. As described in Larson et al. (2019), the counter-gradient flux is a result of updrafts that carry slower momentum ($u' > 0$) across the jet maximum; the momentum flux remains positive until the updraft wind speed has adjusted to the environment at greater heights, even though the local wind gradient has switched sign.

In the meridional component, a jet is present during winter just above the surface layer, along with a roughly 300-m-thick counter-gradient layer above (Fig. 10d–f). In summer, this layer is not present because the meridional wind speed is close to zero. Instead, a thick layer of weak counter-gradient flux is present above 1.9 km (reaching up to about 3 km; not shown).

Finally, we may reconstruct the turbulent momentum flux produced by the K-profile method with input from the model and compare it against the actual resolved fluxes. Following Holtslag and Boville (1993), K may be calculated as:

$$K = \kappa w_m z \left(1 - \frac{z}{h}\right)^2, \tag{8}$$

where $\kappa = 0.4$ is the von Kármán constant, w_m is a turbulent scale velocity and h is the boundary-layer height (here, the cloud-base height). For unstable conditions (such as in the present cases), w_m is proportional to the convective velocity scale w_* (Holtslag and Boville, 1993). Using seasonally averaged surface fluxes (of momentum, heat and moisture) and cloud-base heights h from the simulations, we computed one K profile per season (shown as dotted lines in both Fig. 10c and f). These profiles are used to compute momentum fluxes (shown as dotted lines in Fig. 10b, e).

The K-profile model seems to produce a reasonable estimation of the (subgrid) turbulent stresses, which near the surface are close to the surface momentum fluxes output by the LES (indicated by the coloured tick marks in Fig. 10b, e). However, above 200 m, coherent structures and larger eddies presumably take over much of the transport. It is these fluxes that introduce important tendencies at cloud base.

5 | CONCLUSIONS

In this paper, we utilised a unique set of large-eddy-simulation (LES) hindcasts that were run over the North Atlantic (Stevens et al., 2019) to study the role of convective momentum transport (CMT) and small-scale turbulence in the momentum budget of the trades. To our knowledge, the present study is the first one to disentangle small-scale and coherent convective-scale influences on the momentum budget for different seasons from LES. Because the inner LES domains for which we constructed the momentum budget do not have periodic boundary conditions and have been run at different horizontal resolutions, the data allows a unique view on the relative roles of turbulent stresses and (resolved) flows for a variety of synoptic conditions (in contrast to idealised LES cases).

Asking what the role of shallow convection in the momentum budget of the trades is, our analysis focused on boreal-winter days with steady north-easterly winds and shallow cumulus convection under a strong inversion — thus typical trade-wind conditions — as well as boreal-summer days with weaker winds from the east, somewhat deeper convection and no inversion. In both seasons the combined pressure-gradient and Coriolis force (setting the

geostrophic wind) are of a similar order of magnitude as the combined resolved advection and unresolved turbulent stresses. The influence of 'large-scale' mean horizontal and vertical wind advection appears minor, and we interpret the resolved advection largely as CMT, including thermal and mesoscale circulations that take place in the subcloud and cloud layers. Its structure closely matches that of the vertical divergence of the resolved momentum fluxes.

The combined effect of CMT and unresolved turbulence, which we may label as an ageostrophic or frictional term, is to decelerate the easterly trade winds. Especially in winter, when the wind profile exhibits a strong zonal wind jet near cloud base and larger vertical shear in the easterly wind in the cloud layer, the frictional layer is pronounced and extends up to 2 km. However, CMT has a very different effect depending on the altitude considered: It acts to accelerate near-surface winds, by removing air masses that have gained a westerly component due to surface friction, slow down winds in the central and upper mixed layer and finally, introduce a small amount of 'cumulus friction' in the cloud layer. Notably, CMT introduces little tendency at cloud base where the zonal wind jet resides. By decelerating easterly flow below the jet, it appears to help make the jet more pronounced.

On the other hand, unresolved turbulence introduces a frictional force that is as expected largest near the surface and reduces in magnitude throughout the mixed layer. However, near cloud base and the zonal wind jet, there is significant unresolved turbulence from scales smaller than 150 m that comprise all of the frictional force there. The momentum flux predicted by a K-diffusion model shows that the flux goes to zero about half-way the mixed-layer, which is where the resolved momentum flux peaks, and where dry convective circulations appear to play an important role. Smaller fluxes that correspond to counter-gradient momentum transport are present above the zonal wind jet (in the cloud layer) and meridional wind jet (above the surface layer), which are a result of slower momentum being carried across these wind speed maxima (Larson et al., 2019).

In conclusion, shallow convection plays an important role in the North Atlantic momentum budget, in particular in decelerating easterly winds below cloud base where momentum fluxes converge. 'Cumulus friction' — a term coined by Schneider and Lindzen (1976) to describe a decelerating effect by (deep) convective momentum transport in the cumulus layer — is not readily present here, as cloud fractions appear too small to introduce large fluxes in the cloud layer. However, there is significant friction near cloud base, which appears associated with smaller-scale turbulent stresses introduced by the zonal wind jet and from the clouds themselves.

acknowledgements

We thank Matthias Brueck and Daniel Klocke who ran the ICON-LEM simulations for making available the data and for the support with questions regarding the simulation set-up. The data are archived at the German Climate Computing Center (DKRZ) and can be made available upon request. K.C.H. wishes to thank Bjorn Stevens and Cathy Hohenegger for hosting him at the Max Planck Institute for Meteorology in Hamburg, Germany during parts of this project as well as for inspiring discussions.

conflict of interest

The authors declare no conflicting interests.

references

Augstein, E., Schmidt, H. and Ostapoff, F. (1974) The vertical structure of the atmospheric planetary boundary layer in undisturbed trade winds over the Atlantic Ocean. *Boundary-Layer Meteorology*, **6**, 129–150.

Back, L. E. and Bretherton, C. S. (2009) On the Relationship between SST Gradients, Boundary Layer Winds, and Convergence over the Tropical Oceans. *Journal of Climate*, **22**, 4182–4196.

Bony, S., Stevens, B., Ament, F., Bigorre, S., Chazette, P., Crewell, S., Delanoë, J., Emanuel, K., Farrell, D., Flamant, C., Gross, S., Hirsch, L., Karstensen, J., Mayer, B., Nuijens, L., Ruppert, J. H., Sandu, I., Siebesma, P., Speich, S., Szczap, F., Totems, J., Vogel, R., Wendisch, M. and Wirth, M. (2017) EUREC4A: A Field Campaign to Elucidate the Couplings Between Clouds, Convection and Circulation. *Surveys in Geophysics*, **38**, 1529–1568.

Brueck, M., Nuijens, L. and Stevens, B. (2015) On the seasonal and synoptic time-scale variability of the North Atlantic trade wind region and its low-level clouds. *Journal of the Atmospheric Sciences*, **72**, 1428–1446.

Brümmer, B., Augstein, E. and Riehl, H. (1974) On the low-level wind structure in the Atlantic trade. *Quarterly Journal of the Royal Meteorological Society*, **100**, 109–121.

Carr, M. T. and Bretherton, C. S. (2001) Convective momentum transport over the tropical pacific: Budget estimates. *Journal of the Atmospheric Sciences*, **58**, 1673–1693.

Deser, C. (1993) Diagnosis of the Surface Momentum Balance over the Tropical Pacific Ocean. *Journal of Climate*, **6**, 64–74.

Dipankar, A., Stevens, B., Heinze, R., Moseley, C., Zängl, G., Giorgetta, M. and Brdar, S. (2015) Large eddy simulation using the general circulation model ICON. *Journal of Advances in Modeling Earth Systems*, **7**, 963–986.

Dixit, V., Nuijens, L. and Helfer, K. (2020; in prep.) Counter-gradient momentum transport through subtropical shallow convection in ICON-LEM simulations.

Holland, J. Z. and Rasmusson, E. M. (1973) Measurements of the Atmospheric Mass, Energy, and Momentum Budgets Over a 500-Kilometer Square of Tropical Ocean. *Monthly Weather Review*, **101**, 44–55.

Holtslag, A. A. and Boville, B. A. (1993) Local versus nonlocal boundary-layer diffusion in a global climate model. *Journal of Climate*, **6**, 1825–1842.

Klocke, D., Brueck, M., Hohenegger, C. and Stevens, B. (2017) Rediscovery of the doldrums in storm-resolving simulations over the tropical Atlantic. *Nature Geoscience*, **10**, 891–896.

Larson, V. E., Domke, S. and Griffin, B. M. (2019) Momentum Transport in Shallow Cumulus Clouds and Its Parameterization by Higher-Order Closure. *Journal of Advances in Modeling Earth Systems*, **11**, 3419–3442.

Malkus, J. S. (1958) On the structure of the trade wind moist layer. *Papers in Physical Oceanography and Meteorology*, **13**.

Neggers, R. A., Neelin, J. D. and Stevens, B. (2007) Impact mechanisms of shallow cumulus convection on tropical climate dynamics. *Journal of Climate*, **20**, 2623–2642.

Nuijens, L., Serikov, I., Hirsch, L., Lonitz, K. and Stevens, B. (2014) The distribution and variability of low-level cloud in the North Atlantic trades. *Quarterly Journal of the Royal Meteorological Society*, **140**, 2364–2374.

Riehl, H., Yeh, T. C., Malkus, J. S. and La Seur, N. E. (1951) The north-east trade of the Pacific Ocean. *Quarterly Journal of the Royal Meteorological Society*, **77**, 598–626.

Schneider, E. K. and Lindzen, R. S. (1976) A discussion of the parameterization of momentum exchange by cumulus convection. *Journal of Geophysical Research*, **81**, 3158–3160.

Stevens, B., Ament, F., Bony, S., Crewell, S., Ewald, F., Gross, S., Hansen, A., Hirsch, L., Jacob, M., Kölling, T., Konow, H., Mayer, B., Wendisch, M., Wirth, M., Wolf, K., Bakan, S., Bauer-Pfundstein, M., Brueck, M., Delanoë, J., Ehrlich, A., Farrell, D., Forde, M., Gödde, F., Grob, H., Hagen, M., Jäkel, E., Jansen, F., Klepp, C., Klingebiel, M., Mech, M., Peters, G., Rapp, M., Wing, A. A. and Zinner, T. (2019) A high-altitude long-range aircraft configured as a cloud observatory the narval expeditions. *Bulletin of the American Meteorological Society*, **100**, 1061–1077.

Stevens, B., Duan, J., McWilliams, J. C., Münnich, M. and Neelin, J. D. (2002) Entrainment, Rayleigh friction, and boundary layer winds over the tropical Pacific. *Journal of Climate*, **15**, 30–44.

Stull, R. B. (1988) *An Introduction to Boundary Layer Meteorology*. Dordrecht: Kluwer Academic Publishers, 1st edn.

Tiedtke, M., Heckley, W. A. and Slingo, J. (1988) Tropical forecasting at ECMWF: The influence of physical parametrization on the mean structure of forecasts and analyses. *Quarterly Journal of the Royal Meteorological Society*, **114**, 639–664.

Vial, J., Vogel, R., Bony, S., Stevens, B., Winker, D. M., Cai, X., Hohenegger, C., Naumann, A. K. and Brogniez, H. (2019) A New Look at the Daily Cycle of Trade Wind Cumuli. *Journal of Advances in Modeling Earth Systems*, **11**, 3148–3166.

Zängl, G., Reinert, D., Rípodas, P. and Baldauf, M. (2015) The ICON (ICOsahedral Non-hydrostatic) modelling framework of DWD and MPI-M: Description of the non-hydrostatic dynamical core. *Quarterly Journal of the Royal Meteorological Society*, **141**, 563–579.

GRAPHICAL ABSTRACT

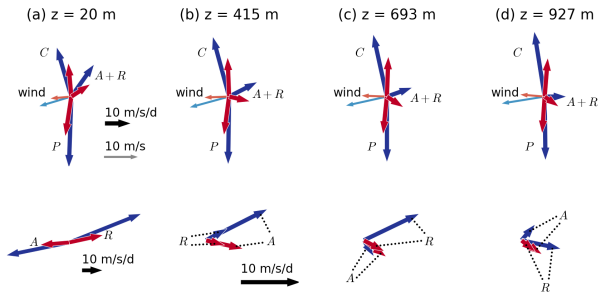

In a novel approach, we use a unique set of LES hindcasts to elucidate the non-negligible role of turbulence and convection in the trade-wind momentum budget. We show that resolved advection and subgrid stresses decelerate the easterly trades within a layer that is 2 km deep in winter and 1 km in summer. Convection in the mixed layer plays an important role in slowing down easterly flow below cloud base (but introduces relatively little 'cumulus friction' in the cloud layer).